

# Less is More: Skim Transformer for Light Field Image Super-resolution

Zeke Zexi Hu<sup>✉</sup>, Haodong Chen<sup>✉</sup>, Hui Ye<sup>✉</sup>, Xiaoming Chen<sup>✉</sup>, Member, IEEE,  
 Vera Yuk Ying Chung<sup>✉</sup>, Member, IEEE, Yiran Shen<sup>✉</sup>, Senior Member, IEEE,  
 Weidong Cai<sup>✉</sup>, Member, IEEE

arXiv:2407.15329v2 [eess.IV] 10 Aug 2025

**Abstract**—A light field image captures scenes through an array of micro-lenses, providing a rich representation that encompasses spatial and angular information. While this richness comes at the cost of significant data redundancy, most existing light field methods still tend to indiscriminately utilize all the information from sub-aperture images (SAIs) in an attempt to harness every visual cue regardless of their disparity significance. However, this paradigm inevitably leads to disparity entanglement, a fundamental cause of inefficiency in light field image processing. To address this limitation, we introduce the Skim Transformer, a novel architecture inspired by the “less is more” philosophy. Unlike conventional light field Transformers, our Skim Transformer features a multi-branch structure where each branch is dedicated to a specific disparity range by constructing its attention score matrix over a skinned subset of SAIs, rather than all of them. Building upon this core component, we present SkimLFSR, an efficient yet powerful network for light field super-resolution (LFSR). Requiring only 67% of parameters, SkimLFSR achieves state-of-the-art results surpassing the best existing method by an average of 0.59 dB and 0.35 dB in PSNR at the 2 $\times$  and 4 $\times$  tasks, respectively. Through in-depth analyses, we reveal that SkimLFSR, guided by the predefined skinned SAI sets as prior knowledge, demonstrates distinct disparity-aware behaviors in attending to visual cues. These findings highlight its effectiveness and adaptability as a promising paradigm for light field image processing.

**Index Terms**—Light field, Super-resolution, Image processing, Deep learning.

## I. INTRODUCTION

Light Field (LF) imaging captures light rays of a scene from multiple angular directions in a single shot, enriching the scene representation and enabling advanced computer vision capabilities such as post-capture refocusing [1], [2], depth estimation [3]–[7], material recognition [8], [9], salient object detection in complex scenes [10]–[12], microscopy [13]–[15], anti-spoofing face recognition [16], [17], and virtual reality (VR) media enhancement [18], [19]. The development of LF acquisition devices spans from early laboratory-built camera arrays [20], [21] to practical cameras, such as Raytrix [22] and

This work was supported in part by National Natural Science Foundation of China (No. 62177001). (Corresponding author: Xiaoming Chen.)

Zeke Zexi Hu, Haodong Chen, Hui Ye, Vera Yuk Ying Chung, and Weidong Cai are with the School of Computer Science, University of Sydney, Darlington, NSW 2008, Australia (E-mail: zexi.hu, haodong.chen, huye0731, vera.chung, tom.cai@sydney.edu.au).

Xiaoming Chen is with the School of Computer Science and Engineering, Beijing Technology and Business University, Beijing 102488, China (E-mail: xiaoming.chen@btbu.edu.cn).

Yiran Shen is with the School of Software, Shandong University, Jinan, 250100, China (E-mail: yiran.shen@sdu.edu.cn).

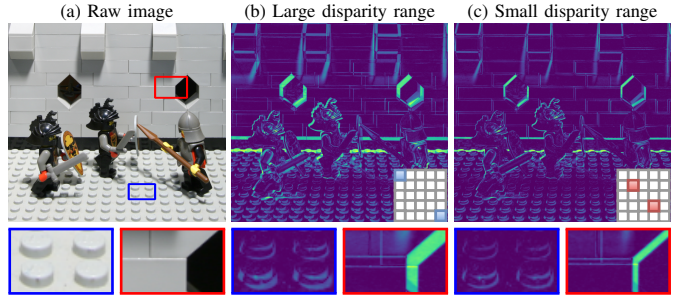


Fig. 1. Parallax at different disparity ranges in the *Lego Knights* sample. The bottom-right indicator in (b) and (c) indicates the SAIs used to obtain the parallax.

Lytro Illum [23], and the more recent panoramic LF system [19] built by Google.

Due to technical limitations, accommodating a large number of micro-lenses within a compact form factor often comes at the cost of spatial resolution in LF images. For instance, the spatial resolution of a Lytro Illum camera is down to 376 $\times$ 541. To mitigate this limitation, several light field image super-resolution (LFSR) methods have been proposed to enhance the spatial resolution while preserving LF’s intrinsic angular structure.

Due to the nature of LF imaging, the angular structure is inherently non-uniform and can vary significantly across different spatial locations and angular directions. These variations arise primarily from two factors: scene depth (from an image-wise perspective) and camera configuration (from a device perspective). Disparity modeling plays a crucial role in harnessing this angular information to achieve effective LFSR.

Fig. 1 exemplifies how parallax manifests differently across disparity ranges. Specifically, Fig. 1(b) demonstrates a larger disparity range by computing the parallax between two outer sub-aperture images (SAIs), making foreground objects such as the Lego studs (highlighted in the blue box) appear more visually prominent. In contrast, Fig. 1(c), which reflects a smaller disparity range using inner SAIs, renders these structures more blurred and indistinct. Conversely, background elements like the brick wall edges (highlighted in the red box) exhibit excessive parallax in Fig. 1(b), whereas they appear sharper and more coherent in Fig. 1(c). These disparities reveal nuanced variations and complexity of disparity distribution in LF images, meanwhile, offering valuable cues for enhancing LFSR performance.

The recent integration of deep learning techniques, especially Vision Transformers (ViT) techniques [24]–[27],

has demonstrated promising potential in leveraging the self-attention mechanism to establish long-range dependencies for spatial, angular, and epipolar plane image (EPI) subspaces in LF images. However, existing Transformer-based methods commonly overlook the substantial disparity variations inherent in LF data. These approaches typically apply self-attention uniformly across the entire LF tensor in a single pass, attempting to exploit all available cues without adequately considering their significance, instead relying on the self-attention mechanism to learn the relevance solely from training data.

In this paper, we identify this issue as disparity entanglement, where heterogeneous disparity cues are processed homogeneously. This not only impairs a LFSR network's ability to model disparity but also introduces computational redundancy.

To address this issue, we propose the Skim Transformer, a novel Transformer architecture grounded in the “**less is more**” philosophy. Rather than indiscriminately processing all SAIs, the Skim Transformer selectively samples a subset of SAIs, referred to as a skimmed SAI set, that serves as prior knowledge to effectively manage disparity information and guide the construction of self-attention. Meanwhile, a multi-branch structure is constructed to broaden this capability to handle diverse disparity ranges. As a result, the Skim Transformer processes less information, but not only mitigates computation redundancy but also disentangles disparity to extract more relevant information.

Building upon Skim Transformers, we present SkimLFSR, an efficient and effective LFSR network that not only delivers superior performance but also improves efficiency through its paradigm of disparity disentanglement. In our experiments, a lightweight variant of SkimLFSR outperforms nearly all existing methods [24], [25], [26] while using only 37% of the parameters, 35% of the FLOPs, and 28% of the inference time. The full version of SkimLFSR surpasses the previous state-of-the-art [27] by a substantial margin of 0.59 dB and 0.35 dB in PSNR for the  $2\times$  and  $4\times$  LFSR tasks, respectively, while requiring just 67% of the parameters used by the prior leading method.

Furthermore, we conduct a series of in-depth analyses to uncover the inner workings of SkimLFSR. The results reveal that SkimLFSR's superior performance originates from its disparity-aware characteristic, as evidenced through deep feature analyses where SkimLFSR exhibits latent discriminative capability toward scene depths and camera configurations. Remarkably, this capability emerges even though neither of these two modalities is explicitly provided as supervision during the regression-based LFSR training, highlighting the effectiveness of Skim Transformer to implicitly capture and exploit underlying disparity cues.

In summary, the contributions of this work are as follows:

- 1) We identify the issue of disparity entanglement in existing Transformer-based LFSR methods, where heterogeneous disparity cues are processed homogeneously, leading to suboptimal performance and computational redundancy.

- 2) We propose the Skim Transformer, a novel architecture built on the “less is more” philosophy. By selectively sampling a skimmed SAI set in its self-attention mechanism and adopting a multi-branch structure, Skim Transformer explicitly targets different disparity ranges and achieves disparity disentanglement in its disparity modeling process.
- 3) Built upon this, we present SkimLFSR, an efficient and high-performing LFSR network. It surpasses the previous leading method by 0.59 dB and 0.35 dB in PSNR for  $2\times$  and  $4\times$  LFSR, respectively, while requiring just 67% of the parameters used by the prior leading method.
- 4) Through in-depth analyses, we reveal that SkimLFSR's superior performance stems from its disparity-aware characteristics and latent discriminative capability toward scene depth and camera configuration, learned implicitly from a regression-based task.

## II. RELATED WORK

### A. Single Image Super-resolution

Single image super-resolution (SISR) is a foundational task in low-level computer vision, aiming to reconstruct a high-resolution (HR) image from a given low-resolution (LR) input. As an upstream research area, advancements in SISR often contribute transferable insights and methodologies to other related domains, including LFSR.

The integration of deep learning into SISR was first introduced by Dong et al. [28] in their SRCNN, the first SISR network based on a convolutional neural network (CNN). It significantly outperformed traditional methods [29], [30], establishing a new paradigm for image processing.

Progress in SISR has since accelerated through a series of architectural innovations. VDSR [31] introduced very deep networks with residual learning to improve data flow in network propagation. RDN [32] enhanced hierarchical feature fusion through dense connections. RCAN [33] further improved representational capacity by incorporating a residual-in-residual structure along with channel attention mechanisms.

Beyond spatial enhancement, researchers have explored the incorporation of auxiliary modalities to enrich the reconstruction process, including spectral priors [34] and language-based guidance via text-to-image models [35]. A distinct line of research has focused on improving perceptual quality, moving beyond traditional pixel-wise fidelity metrics like Pixel-wise Signal-to-Noise Ratio (PSNR). Key developments in this area include the introduction of perceptual loss functions and adversarial learning frameworks [36], [37].

More recently, Transformer-based architectures have gained traction in SISR, motivated by the success of Vision Transformers (ViTs) [38] in high-level vision tasks. Chen et al. [39] proposed a unified IPT Transformer backbone pre-trained across multiple image restoration tasks, demonstrating strong generalization across low-level tasks. SwinIR [40], based on the Swin Transformer [41], introduced a hierarchical design with shifted windows to effectively model both local and global dependencies. HAT [42] extended this paradigm by integrating channel attention with window-based self-attention

to balance fine-grained detail preservation with contextual awareness.

Despite their superior performance, Transformer-based SISR methods are inherently constrained by the quadratic complexity of global self-attention with respect to input resolution, limiting their scalability. To overcome this bottleneck, efficient variants such as SRFormer [43] and ELAN [44] have been proposed. SRFormer employs a permuted self-attention, while ELAN introduces a number of modifications to the self-attention mechanism, including a shifted convolution and sharing attention scores across modules.

The recent emergence of natural language processing (NLP) has also inspired the development of language-assisted SISR methods. For instance, Sun et al. [45], [46] bridged the gap between text and image domains by leveraging diffusion [47], image-to-text [48], [49], and text-to-image [50] models.

Different from SISR, which primarily focuses on restoring visual details degraded during downsampling, LFSR imposes an additional constraint: the preservation and enhancement of angular consistency across SAIs. Moreover, the computation and memory constraints of LFSR are more severe than those of SISR, due to the higher dimensionality of LF data. These unique challenges motivate the development of dedicated LFSR methods.

### B. Light Field Image Super-resolution

Processing 4D LF images introduces substantial challenges for neural network design due to their high dimensionality and the intricate spatial-angular dependencies they encode. A naive solution is to apply 4D convolutions directly. However, it incurs prohibitively intensive computation, making both training and inference impractical, and it often suffers from optimization difficulties due to the overwhelming data complexity [51].

To alleviate these issues, decomposition-based strategies have gained prominence in the LF community. Wang et al. [8] introduced the interleaved filter for LF material recognition, which approximates 4D convolutions by decomposing them into separate spatial and angular convolutions. This technique achieved comparable performance to full 4D convolutions while substantially reducing computational overhead, laying the groundwork for efficient LF representation learning.

This decomposition paradigm was subsequently adapted for LFSR by Yoon et al. [52] in their LFCNN consisting of two separate sub-networks. Yeung et al. [53] further improve this paradigm by making the network end-to-end. Building on these foundations, Jin et al. [54] introduced an all-to-one strategy, where each SAI is super-resolved using contextual information from all other SAIs, with a structure-aware loss to preserve parallax. Wang et al. [55] proposed a two-branch network that separately extracts spatial and angular features and fuses them iteratively. Liu et al. [56] further improved angular-spatial modeling by incorporating dilated convolutions in a multi-scale pyramid structure to expand receptive fields across spatial and angular subspaces. Chen et al. [57] explored an approach incorporating frequency-domain learning and semantic priors.

Given that LF images inherently encompass multiple subspaces, the decomposition paradigm is extended beyond the spatial and angular subspaces. Cheng et al. [58] proposed LFSSR-SAV, which employs spatial-angular versatile convolution to handle EPI subspaces. Hu et al. [59] generalized this idea with the Decomposition Kernel Network (DKNet), jointly modeling spatial, angular, and EPI subspaces. Wang et al. [60] introduced a disentanglement mechanism to better aggregate and refine multi-subspace features, while Duong et al. [61] proposed a hybrid model that integrates multi-orientation EPI extractors with angular and spatial representation extractors.

Parallel to advancements in SISR, the ViT technique has expanded its successes to LFSR. Wang et al. [62] proposed DPT equipped with content and gradient Transformers to build long-range dependencies within the spatial subspace. Liang et al. [26] employed self-attention on overlapped local windows in their spatial Transformers, akin to HAT [42] for SISR. Transformers are also extended to the EPI subspaces in EPIT [24]. Cong et al. proposed LF-DET [25], integrating a sub-sampling spatial strategy and a multi-scale angular modeling strategy to enhance spatial and angular modeling. Hu et al. [27] proposed M2MTNet with Many-to-Many Transformers that avoid the practice of merging subspaces into the batch dimension and resolve the broadly existing issue of subspace isolation.

Despite these recent advancements, as discussed in the previous section, a key limitation remains: most existing methods treat all the LF clues equally within attention modules, leading to disparity entanglement. To address this issue, we propose the Skim Transformer, a novel disparity-aware architecture that selectively attends to relevant information.

## III. METHODOLOGY

### A. Preliminaries

The task of LFSR is to enhance the spatial resolution of a low-resolution (LR) LF image  $I_{LR}$  to produce a super-resolved (SR) LF image  $I_{SR}$ , which aims to approximate the corresponding high-resolution (HR) LF image  $I_{HR}$ :

$$I_{SR} = \mathcal{F}(I_{LR}), \quad I_{LR} \in \mathbb{R}^{U \times V \times W \times H \times C}, \\ I_{SR} \in \mathbb{R}^{U \times V \times rW \times rH \times C} \quad (1)$$

where  $\mathcal{F}(\cdot)$  is the LFSR function,  $(U \times V)$  and  $(W \times H)$  represent the angular and spatial subspaces of a LR image, respectively. The term  $r$  denotes the LFSR scale.

### B. Network Architecture

The proposed SkimLFSR network is illustrated in Fig. 2. The network comprises three primary stages: initial feature extraction, deep feature extraction, and image generation. The initial feature extraction stage utilizes four consecutive  $3 \times 3$  convolution layers operating on the spatial subspace of LF images to obtain low-level features. The subsequent deep feature extraction stage incorporates a sequence of  $N_{CB}$  correlation blocks to derive comprehensive correlation information and establish a high-level spatial-angular representation. Their details will be elaborated on in the following paragraphs.

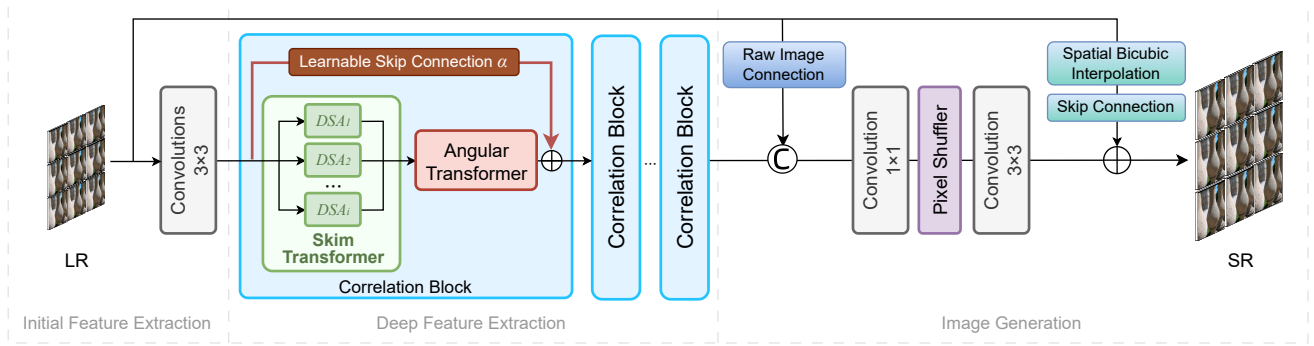


Fig. 2. Illustration of the SkimLFSR network.

The final image generation stage aggregates the deep features via convolution layers and upsamples the spatial resolution through a pixel shuffler [63] to produce the final LF image output.

**Correlation Blocks.** The correlation block comprises two specialized Transformers: the Skim Transformer, which operates in the spatial subspace, and the angular Transformer, which focuses on the angular subspace. The angular Transformer follows the methodologies of prior works [25], [26] at large, utilizing a vanilla Transformer to build long-range dependencies in the angular subspace with each SAI as a token.

These Transformers are preceded by two  $3 \times 3$  spatial convolutions serving as positional encoding [64], and followed by a channel attention mechanism [33] for channel-wise enhancement.

**Connection Enhancement.** To improve SkimLFSR’s data flow, besides a standard skip connection that bridges the SR and LR, two extra connections are integrated, as illustrated in Fig. 2. Firstly, in alignment with the strategy from DKNet [59], a raw image connection concatenates the raw image tensor directly to the output of the last correlation block prior to the image generation stage. This connection acts as a special form of dense connections [65], ensuring that raw image data directly contributes to feature aggregation and upsampling. Secondly, inspired by RGT [66], each correlation block incorporates a learnable skip connection that dynamically adjusts the input by channel-wise coefficients  $\alpha \in \mathbb{R}^C$  and adds it to the output. These two connections incur negligible computational overhead but usually improve the SkimLFSR’s performance by about 0.1 dB PSNR in the experiments.

### C. Skim Transformer

In this subsection, we present the core component of SkimLFSR, Skim Transformers. An illustration is presented in Fig. 3. It features a multi-branch structure to target different disparity ranges.

Given a 4D LF tensor  $\mathbf{X} \in \mathbb{R}^{U \times V \times W \times H \times C}$ , the channels are at first split evenly into  $N_{DSA}$  branches, with each branch  $X_i$  holding  $C/N_{DSA}$  channels. Each  $X_i \in \mathbb{R}^{U \times V \times W \times H \times C/N_{DSA}}$  will undergo Disparity Self-attention  $DSA_i$  to explicitly construct long-range dependencies for a specific disparity range.

**Matrix Projection.** To achieve this, diverging from conventional LF Transformers [24]–[26], we introduce two substantial revamps for the matrix projection of query, key, and value matrices:

First, the query and key matrices, denoted as  $Q_i$  and  $K_i$ , are constructed on a skinned SAI set  $\bar{X}_i$  holding  $S_i$  SAIs out of the full SAI set  $\{U \times V\}$ , i.e.  $\{S_i\} \subseteq \{U \times V\}$ . This skimming process will serve as a selective sampling of the angular subspace to target specific disparity ranges.

Second, to facilitate a 4D LF tensor to be processed by the 1D self-attention mechanism, conventional LF Transformers typically merge the angular subspace with the batch dimension, treating the spatial subspace as tokens and the channel dimension as embedding, i.e.  $\bar{X}_i \in \mathbb{R}^{UV \times WH \times C'}$  ( $C' = C/N_{DSA}$ ). In contrast, the proposed Disparity Self-attention  $DSA_i$  merges the angular subspace with the channel dimension, resulting in a LF tensor  $\bar{X}_i \in \mathbb{R}^{WH \times S_i C'}$ , with the spatial subspace remained as tokens, the merged channel dimension representing the disparity information, and the batch dimension omitted. This design enables the subsequent disparity embedding process to encode disparities implicitly.

**Disparity Embedding.** Disparity embedding is accomplished via a linear layer  $D_i$  projecting from  $\mathbb{R}^{S_i C/N_{DSA}}$  to  $\mathbb{R}^{C_D}$  to produce a compact disparity embedding  $\mathcal{D}_i \in \mathbb{R}^{WH \times C_D}$ . This embedding is then fed to two linear layers,  $Q_i$  and  $K_i$ , each of which projects from  $\mathbb{R}^{C_D}$  to  $\mathbb{R}^{C_{QK}}$ , to generate the query and key matrices  $Q_i$  and  $K_i$ , respectively. On the other hand, the value matrix,  $V_i$ , is directly derived from  $X_i$ , thus preserving the entire angular information with the full SAI set.

**Self-attention Output.** As a result, the process for obtaining these three matrices for self-attention is formally expressed as follows:

$$\begin{aligned} Q_i &= Q_i(\mathcal{D}_i), \quad K_i = K_i(\mathcal{D}_i), \quad V_i = X_i, \\ \mathcal{D}_i &= D_i(\bar{X}_i); \\ X_i &\in \mathbb{R}^{U \times V \times W \times H \times C/N_{DSA}}; \\ \bar{X}_i &\in \mathbb{R}^{WH \times S_i C/N_{DSA}}, \quad \{S_i\} \subseteq \{U \times V\}; \\ Q_i, K_i : \mathbb{R}^{C_D} &\mapsto \mathbb{R}^{C_{QK}}, \quad D_i : \mathbb{R}^{S_i C/N_{DSA}} \mapsto \mathbb{R}^{C_D}. \end{aligned}$$

With the obtained query, key, and value matrices, the upcoming self-attention calculation, including attention score

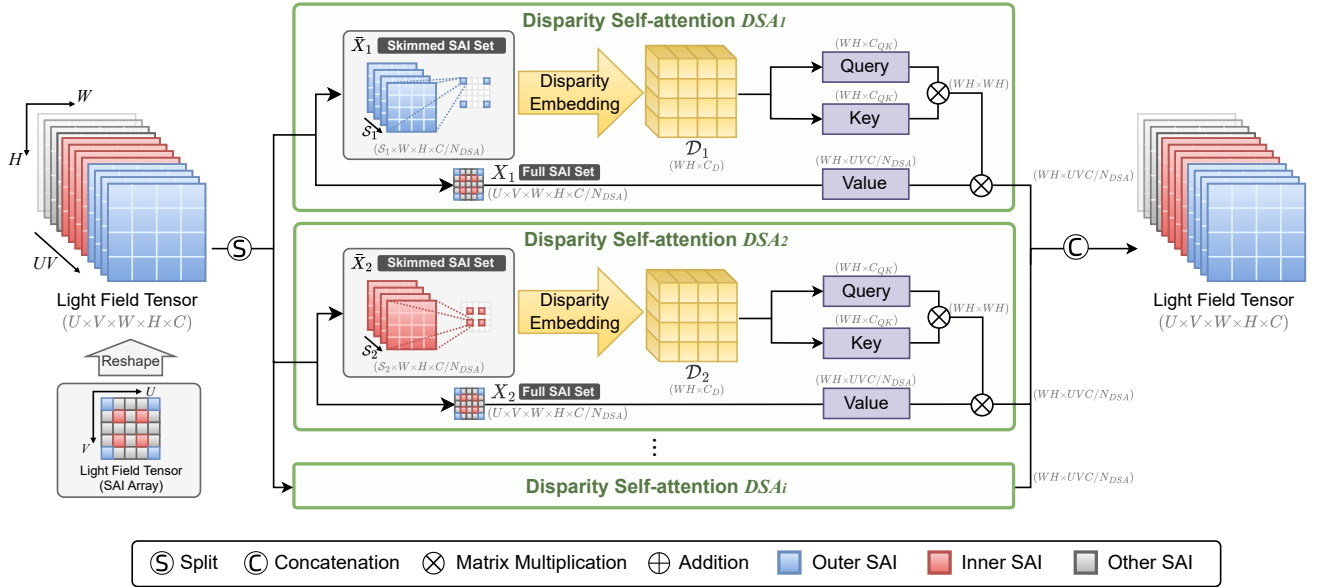


Fig. 3. Illustration of Skim Transformer.

matrix and self-attention output, follows the typical Transformer method:

$$DSA_i(\mathcal{Q}_i, \mathcal{K}_i, \mathcal{V}_i) = \text{Softmax}(\mathcal{Q}_i \mathcal{K}_i^T / \sqrt{C_{QK}}) \mathcal{V}_i,$$

where  $DSA_i \in \mathbb{R}^{WH \times UVC/N_{DSA}}$ . Note that as the channel number is made consistent as  $C/N_{DSA}$  through the Skim Transformer, the shape of self-attention output aligns with the input, therefore, channel projection is not necessary, and the feed-forward network can be removed to reduce the computation.

Finally, DSA's output is compiled by concatenation as the final output of the Skim Transformer ( $SkimT$ ):

$$\mathbf{Y} = SkimT(\mathbf{X}) = [DSA_1, DSA_2, \dots, DSA_{N_{DSA}}]$$

where  $[\cdot]$  signifies the concatenation operation, and  $\mathbf{Y} \in \mathbb{R}^{WH \times UVC}$  and finally  $\mathbf{R}^{U \times V \times W \times H \times C}$ .

#### D. Discussion

With these innovations, the Skim Transformer confers three principal advantages:

First, Skim Transformers systematically disentangle the process of disparity modeling via a divide-and-conquer strategy. It splits the task into multiple DSA branches, each serving as a specialized prior and constructing its own attention score matrix over a selectively skimmed SAI subset in the query and key matrices to target specific disparity ranges. By ensuring each branch operates separately, any specific disparity, especially those underrepresented in training samples yet critical for high-fidelity reconstructions, is preserved from being overlooked and suppressed. This architecture enables SkimLFSR to become inherently disparity-aware. Further analysis in Sections IV-E1 and IV-E2 investigates how this design correlates with scene depth and camera configurations in LF images. Although these two modalities are not explicitly provided during regression-based training, SkimLFSR appears to develop a discriminative tendency aligned with them.

Second, the Skim Transformer offers flexibility in the construction of skimmed SAI sets, enabling customized attention for any desired disparity range. As illustrated in Fig.3, the  $DSA_1$  branch leverages the outer SAIs at the corners to model larger disparities, while  $DSA_2$  employs inner SAIs for shorter disparity modeling. Both the number and spatial configuration of SAIs can vary between branches and may overlap. Regardless of the configuration, the resulting tokens remain in the spatial domain ( $W \times H$ ), ensuring that the computed attention matrices maintain a shape of  $(WH \times WH)$  before being applied to the value matrix. This flexibility allows the network for meeting diverse requirements and scenarios. In Section IV-E3, we experiment with a variety of SAI combinations to showcase this flexibility and analyze the rationale behind SAI selection in maximizing the performance.

Third, the Skim Transformer significantly reduces computational redundancy without information loss. This is achieved by applying the skimming process only to the query  $\mathcal{Q}_i$  and key  $\mathcal{K}_i$  matrices to compute the attention score matrix, while the value matrix  $\mathcal{V}_i$  retains the full set of SAIs. As a result, the revised self-attention mechanism still preserves full access to LF information while substantially lowering computational cost. In other words, the principle of “less” is realized not at the expense of losing information.

Table I presents a theoretical computation complexity comparison between a Skim Transformer ( $SkimT$ ) and a conventional spatial Transformer ( $T$ ) [25]. The overall complexity is broken down into four components: matrix projection, attention score matrix, self-attention output, and feed-forward network.

Assuming  $U = V = 5$ ,  $S_i = 4$ ,  $C_D = 2C$ ,  $C_{QK} = C$ , and  $N_{DSA} = 2$  (as used in the experiments), the Skim Transformer substantially brings computation complexity down as follows:

- 1) **Matrix Projection:** Conventional spatial Transformers compute dense projections ( $\mathbb{R}^C \mapsto \mathbb{R}^C$ ), resulting in a cost of  $\mathcal{O}(C^2)$  for all  $(U \times V)$  SAIs and three

TABLE I

COMPARISON OF THEORETICAL COMPUTATION COMPLEXITY BETWEEN A CONVENTIONAL SPATIAL TRANSFORMER AND A SKIM TRANSFORMER.

	$\mathcal{C}(T)$	$\mathcal{C}(SkimT)$	$\mathcal{C}(SkimT)/\mathcal{C}(T)$ [Symbolic]	$\mathcal{C}(SkimT)/\mathcal{C}(T)$ [Numeric]
(1) Matrix Projection	$3UVWHC^2$	$\sum_{i=1}^{N_{DSA}} S_i WH \left( \frac{C}{N_{DSA}} C_D + 2C_D C_{QK} \right)$	$\frac{\sum_{i=1}^{N_{DSA}} S_i (C_D C / N_{DSA} + 2C_D C_{QK})}{3UV C^2}$	$40 : 75 \approx 53\%$
(2) Attention Score Matrix	$UV(WH)^2 C$	$N_{DSA} (WH)^2 C_{QK}$	$\frac{N_{DSA} C_{QK}}{UVC}$	$2 : 25 \approx 8\%$
(3) Self-attention Output	$UV(WH)^2 C$	$UV(WH)^2 C$	$1 : 1$	$1 : 1 = 100\%$
(4) Feed-forward Network	$UVWHC^2$	0	$0 : 1$	$0 : 1 = 0\%$

\* Note:  $\mathcal{C}(T)$  and  $\mathcal{C}(SkimT)$  denotes the computation complexity of a conventional spatial Transformer and a Skim Transformer, respectively.

times for the query, key, and value matrices. In contrast, each DSA branch performs disparity embedding  $\mathcal{O}(\frac{C}{N_{DSA}} C_D)$  once, followed by linear projections of  $\mathcal{O}(2C_D C_{QK})$  twice for the query and key matrices. More importantly, the angular complexity are reduced from  $\mathcal{O}(UV)$  to  $\mathcal{O}(S_i)$ . As a result, the required computation complexity is reduced to only 53%.

- 2) **Attention Score Matrix:** The attention score matrix in conventional spatial Transformer calculates the  $(WH \times WH)$  matrix by performing a dot product between the query and key matrices derived from the full LF tensors  $\mathbb{R}^{U \times V \times W \times H \times C}$ . This operation incurs a spatial complexity  $\mathcal{O}((WH)^2)$ , repeated across SAIs  $\mathcal{O}(UV)$  and channels  $\mathcal{O}(C)$ . By comparison, the Skim Transformer encodes the angular subspace into the channel dimension via disparity embedding, effectively eliminating redundant computation in the angular subspace. Consequently, its angular complexity scales linearly with  $\mathcal{O}(N_{DSA})$  and instead of  $\mathcal{O}(UV)$ , and the channel complexity remains  $\mathcal{O}(C_{QK})$  (with  $C_{QK} = C$ ). As we adopt  $N_{DSA} = 2$  in our experiments, the overall complexity is significantly reduced to only 8% of the original.
- 3) **Self-attention Output:** The self-attention output involves a matrix multiplication between the attention score matrix and the value matrix. This step is identical for both the spatial Transformer and the Skim Transformer, and thus they share the same computational complexity  $\mathcal{O}(UV(WH)^2 C)$  in this part.
- 4) **Feed-forward Network:** Since the shape of the Skim Transformer's self-attention output matches its input, there is no need for a feed-forward network for channel projection, unlike in conventional spatial Transformers. This leads to a complete computation reduction from  $\mathcal{O}(UVWHC^2)$  to  $\mathcal{O}(0)$ .

These optimizations contribute to the Skim Transformer's substantial improvement in efficiency, as further demonstrated in Section IV-D and Fig. 6.

## IV. EXPERIMENTS

### A. Experimental Settings

We conduct experiments using the widely adopted BasicLFSR framework [67] and following its protocol. It consists of five datasets: *EPFL* [68], *HCInew* [69], *HCIold* [70], *INRIA* [71], and *STFgantry* [21]. These datasets are split into 70/20/10/35/9 training samples and 10/4/2/5/2 testing samples,

respectively. As per the protocol [67], only the central  $5 \times 5$  SAIs are used. During training, each SAI is divided into patches of size  $64 \times 64$  or  $128 \times 128$  to form HR patches, and the corresponding LR patches are generated via bicubic down-sampling by factors of  $1/2$  or  $1/4$ , corresponding to the  $2 \times$  and  $4 \times$  LFSR scales. We adopt the  $L_1$  loss function and the Adam optimizer with a learning rate of  $2 \times 10^{-4}$  and a batch size of 4. The network is trained for 100 epochs, followed by an additional 10 epochs for fine-tuning with a learning rate of  $2 \times 10^{-5}$ .

Regarding SkimLFSR's hyperparameters, we empirically set the feature channels  $C = 48$  across all Transformers and convolutions, and  $C_D = 96$  and  $C_{QK} = 48$  for Skim Transformers. Within each Skim Transformer, as shown in Fig. 3, we employ two DSA branches ( $N_{DSA} = 2$ ), one of which leverages the four outer SAIs (blue) representing the largest disparity range, and the other one uses the four inner SAIs (red) closer to the center for the smaller disparity range. Due to the improved efficiency of Skim Transformers, we can construct a deeper network with 20 correlation blocks ( $N_{CB} = 20$ ) for both the  $2 \times$  and  $4 \times$  LFSR scale.

The experiments are conducted on a workstation equipped with an Intel i7-11700 4.80GHz 8-core CPU, 32 GB RAM, and an NVIDIA RTX 3090 GPU. The implementation code and trained models will be publicly available at <https://huzexi.github.io/>.

### B. Quantitative Comparison

A quantitative comparison is conducted to compare the overall performance of SkimLFSR with state-of-the-art methods at the  $2 \times$  and  $4 \times$  scales. PSNR and SSIM are calculated on the *Y* channel of the *YCbCr* color space as the quantitative metrics of model performance.

The comparative evaluation encompasses both convolution-based and Transformer-based approaches. The convolution-based methods include LFSSR [53], LF-ATO [54], LF-InterNet [55], LF-IIINet [56], DKNet [59], LFSSR-SAV [58], DistgSSR [60], and HLFSSR [61]. The Transformer-based methods comprise DPT [62], LFT [26], EPIT [24], LF-DET [25], and M2MT-Net [27].

The quantitative results presented in Table II demonstrate that SkimLFSR achieves superior performance across both  $2 \times$  and  $4 \times$  scales on all five datasets. Specifically, SkimLFSR attains an average performance advantage of 0.59 dB and 0.35 dB PSNR over the second-best M2MT-Net at  $2 \times$  and  $4 \times$  scales, respectively. When examining individual datasets,

TABLE II  
COMPARISON OF PSNR/SSIM. THE BEST AND SECOND-BEST RESULTS ARE HIGHLIGHTED IN BOLD AND UNDERLINED, RESPECTIVELY.

Methods	EPFL (70/10)	HCInew (20/4)	HCIdold (10/2)	INRIA (35/5)	STFgantry (9/2)	Average
<b>2× LFSR</b>						
LFSSR [53]	33.67/0.9744	36.80/0.9749	43.81/0.9938	35.28/0.9832	37.94/0.9898	37.50/0.9832
LF-ATO [54]	34.27/0.9757	37.24/0.9767	44.21/0.9942	36.17/0.9842	39.64/0.9929	38.31/0.9848
LF-InterNet [55]	34.11/0.9760	37.17/0.9763	44.57/0.9946	35.83/0.9843	38.44/0.9909	38.02/0.9844
LF-IIINet [56]	34.73/0.9773	37.77/0.9790	44.85/0.9948	36.57/0.9853	39.89/0.9936	38.76/0.9860
DKNet [59]	34.01/0.9759	37.36/0.9780	44.19/0.9942	35.80/0.9843	39.59/0.9910	38.19/0.9847
DPT [62]	34.49/0.9758	37.36/0.9771	44.30/0.9943	36.41/0.9843	39.43/0.9926	38.40/0.9848
LFSSR-SAV [58]	34.62/0.9772	37.42/0.9776	44.22/0.9942	36.36/0.9849	38.69/0.9914	38.26/0.9851
DistgSSR [60]	34.81/0.9787	37.96/0.9796	44.94/0.9949	36.58/0.9859	40.40/0.9942	38.94/0.9867
LFT [26]	34.78/0.9776	37.77/0.9788	44.63/0.9947	36.54/0.9853	40.41/0.9941	38.82/0.9861
HLFSR [61]	35.31/0.9800	38.32/0.9807	44.98/0.9950	37.06/0.9867	40.85/0.9947	39.30/0.9874
EPIT [24]	34.85/0.9775	38.23/0.9810	45.08/0.9949	36.68/0.9852	42.17/0.9957	39.40/0.9869
LF-DET [25]	35.20/0.9794	38.22/0.9803	44.92/0.9949	36.88/0.9862	41.56/0.9953	39.36/0.9872
M2MT-Net [27]	35.64/0.9815	38.43/0.9810	45.38/0.9953	37.22/0.9870	40.99/0.9949	39.53/0.9879
SkimLFSR (Ours)	<b>36.08/0.9834</b> +0.44/+0.0019	<b>38.83/0.9823</b> +0.40/+0.0013	<b>45.66/0.9955</b> +0.28/+0.0002	<b>37.55/0.9881</b> +0.33/+0.0011	<b>42.50/0.9962</b> +0.33/+0.0005	<b>40.12/0.9891</b> +0.59/+0.0012
<b>4× LFSR</b>						
LFSSR [53]	28.60/0.9118	30.93/0.9145	36.91/0.9696	30.59/0.9467	30.57/0.9426	31.52/0.9370
LF-ATO [54]	28.51/0.9115	30.88/0.9135	37.00/0.9699	30.71/0.9484	30.61/0.9430	31.54/0.9373
LF-InterNet [55]	28.81/0.9162	30.96/0.9161	37.15/0.9716	30.78/0.9491	30.36/0.9409	31.61/0.9388
LF-IIINet [56]	29.04/0.9188	31.33/0.9208	37.62/0.9734	31.03/0.9515	31.26/0.9502	32.06/0.9429
DKNet [59]	28.85/0.9174	31.17/0.9185	37.31/0.9720	30.80/0.9501	30.85/0.9460	31.80/0.9408
DPT [62]	28.94/0.9170	31.20/0.9188	37.41/0.9721	30.96/0.9503	31.15/0.9488	31.93/0.9414
LFSSR-SAV [58]	29.37/0.9223	31.45/0.9217	37.50/0.9721	31.27/0.9531	31.36/0.9505	32.19/0.9439
DisgSSR [60]	28.99/0.9195	31.38/0.9217	37.56/0.9732	30.99/0.9519	31.65/0.9534	32.12/0.9439
LFT [26]	29.33/0.9196	31.36/0.9205	37.59/0.9731	31.30/0.9515	31.62/0.9530	32.24/0.9436
HLFSR [61]	29.20/0.9222	31.57/0.9238	37.78/0.9742	31.24/0.9534	31.64/0.9537	32.28/0.9455
EPIT [24]	29.31/0.9196	31.51/0.9231	37.68/0.9737	31.35/0.9526	32.18/0.9570	32.41/0.9452
LF-DET [25]	29.42/0.9220	31.51/0.9227	37.76/0.9739	31.34/0.9528	32.02/0.9561	32.41/0.9455
M2MT-Net [27]	<u>29.85/0.9284</u>	<u>31.76/0.9264</u>	<u>37.98/0.9749</u>	<u>31.77/0.9563</u>	<u>32.20/0.9584</u>	<u>32.71/0.9489</u>
SkimLFSR (Ours)	<b>30.06/0.9308</b> +0.21/+0.0024	<b>32.03/0.9289</b> +0.27/+0.0025	<b>38.26/0.9762</b> +0.28/+0.0013	<b>31.92/0.9572</b> +0.15/+0.0009	<b>33.00/0.9630</b> +0.80/+0.0046	<b>33.06/0.9512</b> +0.35/+0.0023

<sup>+</sup> Note: The number pair below each dataset represents the number of training/testing samples.

the performance gains range from a minimum of 0.28 dB PSNR on the *HCIdold* dataset at the 2× scale and 0.15 dB PSNR on *INRIA* at the 4× scale. A particularly strong performance is observed at the 2× scale on the *EPFL* dataset, with SkimLFSR achieving a gain of 0.44 dB, and an even greater improvement of 0.80 dB on the *STFgantry* dataset at the 4× scale. This substantial improvement aligns with our hypothesis that the disparity disentanglement capability of Skim Transformers enables SkimLFSR to effectively handle diverse disparity ranges and deliver a balanced performance. This advantage is particularly pronounced on the severely underrepresented *STFgantry* dataset as it features larger disparity ranges but contains only nine training samples, representing merely 6.25% of the total 144 training samples, making it the most data-scarce subset in our evaluation.

To provide additional insight into SkimLFSR's comparative advantages, we present a radar plot in Fig. 4. At the 2× scale, although EPIT exhibits strong performance on the large-disparity *STFgantry* dataset, this appears to result from overfitting to large disparity ranges, as evidenced by its substantial performance degradation on other datasets featuring smaller disparity ranges, such as *EPFL* and *INRIA*. Similarly, at the

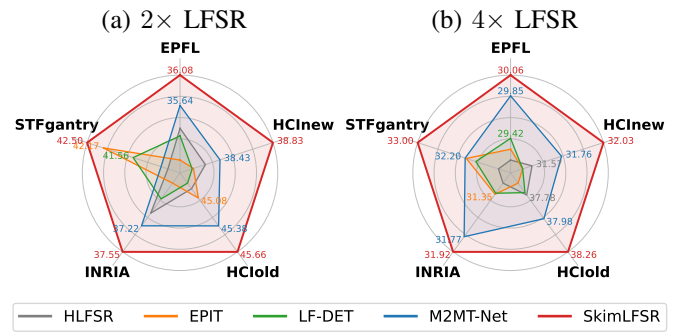


Fig. 4. Comparison of PSNR on the five testing datasets.

4× scale, while M2MT-Net demonstrates competitive performance across most datasets, it achieves only limited gains on *STFgantry*. These observations highlight the challenge faced by existing LFSR networks in maintaining consistently strong performance across various disparity ranges. In contrast, no competing method matches our SkimLFSR's performance on any individual dataset, underscoring its robustness and ability to effectively manage the balance of diverse disparity

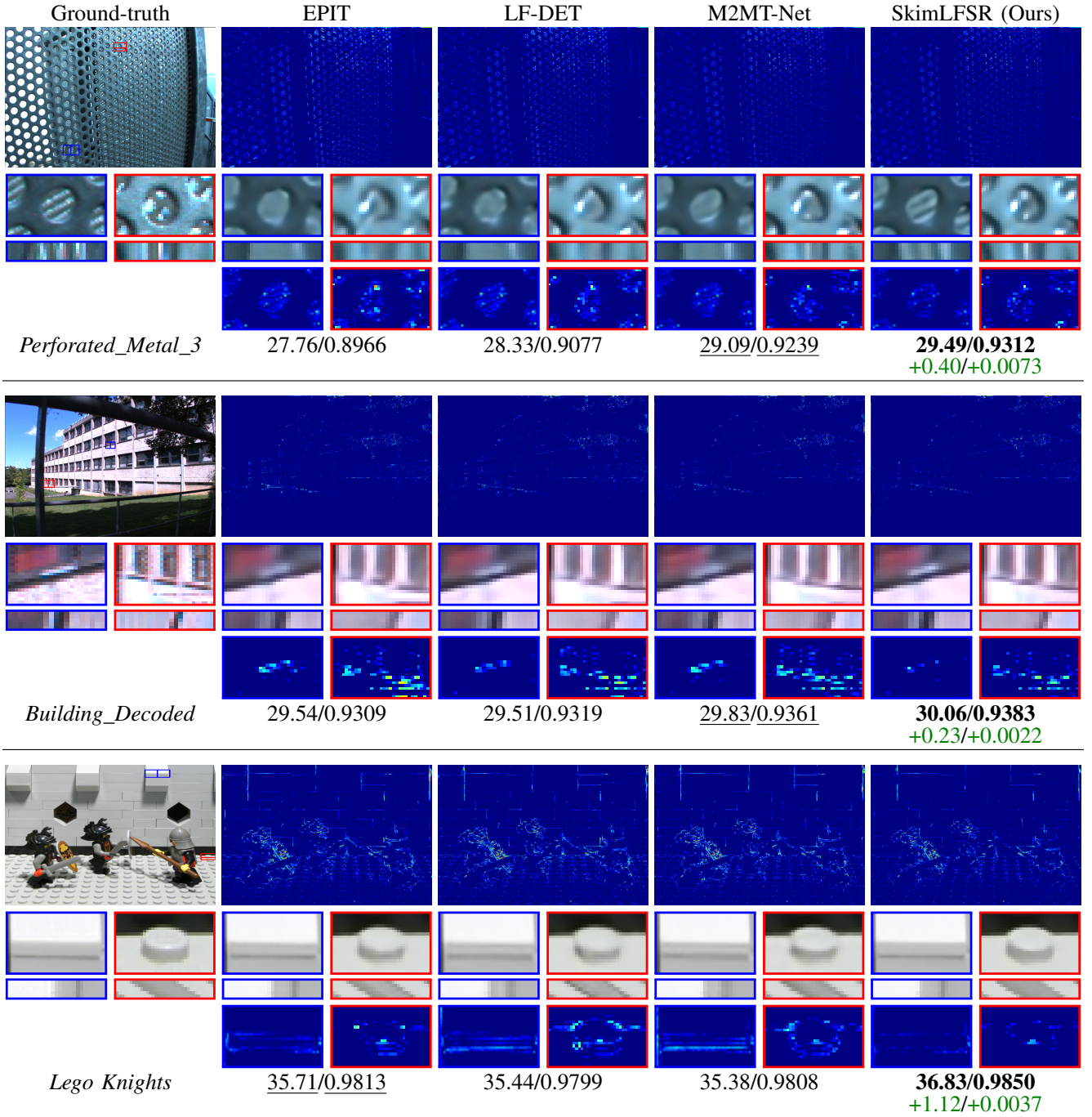


Fig. 5. Qualitative comparison of  $4\times$  LFSR on samples. For each sample, the first row displays the ground-truth image and corresponding error maps for each method. The second row presents zoom-in views of regions highlighted by blue and red bounding boxes, accompanied by their respective EPIs. The third row shows error maps of the zoom-in regions. The bottom row shows the sample name and PSNR/SSIM values.

conditions.

### C. Qualitative Comparison

We showcase SkimLFSR's superior performance through qualitative evaluations at the  $4\times$  scale in Fig. 5.

The first example, shown in (a) *Perforated\_Metal\_3*, is a real LF image from the EPFL dataset captured with a Lytro Illum camera. This challenging scene features complex occlusion patterns with dense perforations and bright light spots. SkimLFSR's reconstruction exhibits remarkable detail

preservation, as evidenced in the blue region where light spot details emerge clearly, and in the red region where both light spots and hole edges are sharply delineated. In contrast, competing methods suffer from light leakage artifacts around bright spots and produce indistinct hole boundaries. The corresponding EPIs further confirm that SkimLFSR maintains superior detail fidelity and angular consistency compared to alternative approaches. As a result, SkimLFSR achieves a 0.40 dB PSNR improvement over the second-best M2MT-Net.

Similar improvements are observed in (b)

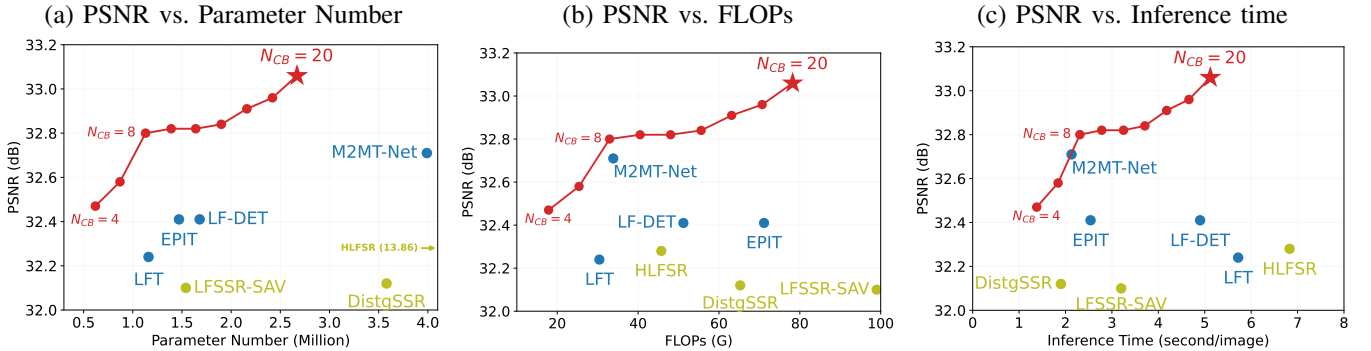


Fig. 6. Trade-off between PSNR (the vertical axis) and model efficiency (the horizontal axis). Transformer-based methods are marked with blue dots, CNN-based methods are marked with yellow dots. The series of SkimLFSR variants are marked with red dots and connected with lines. Methods closer to the top right corner indicate better performance and efficiency.

*Building\_Decoded* from the INRIA dataset, also captured with a Lytro Illum camera. SkimLFSR attains a 0.23 dB PSNR gain over the runner-up M2MT-Net. The error maps within the highlighted regions reveal that this performance enhancement stems from more accurate edge reconstruction and reduced artifacts along building window boundaries. The zoom-in views and EPIs corroborate these findings, showing notably sharper window edges in SkimLFSR’s output.

(c) *Lego Knights* is a synthetic sample from the *STFgantry* dataset, where SkimLFSR achieves the most substantial improvement of 1.12 dB PSNR over the second-best EPIT. The reconstruction quality differences are particularly evident in the slim lines in the background. The blue box highlights one of these regions. This exemplifies SkimLFSR’s capability to accurately handle fine details with small disparities in the background. The foreground reconstruction also benefits from SkimLFSR’s ability, as depicted in the red box, where the stud edges are reconstructed with substantially lower error magnitudes in SkimLFSR’s error map.

These examples collectively validate SkimLFSR’s exceptional ability to reconstruct fine details across diverse disparity ranges and structural characteristics, maintaining consistent performance advantages in both foreground and background regions.

#### D. Model Efficiency

We assess the efficiency of SkimLFSR by benchmarking it against state-of-the-art methods at the  $4\times$  scale. To assess performance across a spectrum of model complexities, we vary the number of correlation blocks  $N_{CB}$  from 4 to 20 in increments of two. The compared methods include the Transformer-based LFT [26], EPIT [24], LF-DET [25] and M2MT-Net [27], as well as the convolution-based DistgSSR [60], LFSSR-SAV [58] and HLFSR [61]. The results are presented in Table III and plotted in Fig. 6. In the plots, the average PSNR is used as the performance metric on the vertical axis. Three efficiency metrics are involved as the horizontal axis: (a) parameter number, (b) FLOPs, and (c) inference time. The parameter number is measured in millions (M), indicating model size, FLOPs (floating-point operations) are measured in billions (G), indicating theoretical

TABLE III  
MODEL EFFICIENCY AND PERFORMANCE OF SKIMLFSR AND STATE-OF-THE-ART METHODS AT THE  $4\times$  SCALE. THE BEST RESULTS ARE HIGHLIGHTED IN BOLD.

Method	#Params. (Million)	FLOPs (G)	Time (s)	PSNR/SSIM
LFSSR-SAV [58]	1.54	99.45	3.20	32.19/0.9439
DistgSSR [60]	3.58	65.26	1.89	32.12/0.9439
HLFSR [61]	13.86	45.73	6.83	32.28/0.9455
LFT [26]	1.16	30.42	5.72	32.24/0.9436
EPIT [24]	1.47	71.15	2.54	32.41/0.9452
LF-DET [25]	1.68	51.20	4.90	32.41/0.9455
M2MT-Net [27]	3.99	33.85	2.13	32.71/0.9489
SkimLFSR (Ours)				
$N_{CB} = 4$	<b>0.62</b>	<b>17.85</b>	<b>1.38</b>	32.47/0.9456
$N_{CB} = 6$	0.87	25.39	1.84	32.58/0.9474
$N_{CB} = 8$	1.13	32.94	2.31	32.80/0.9486
$N_{CB} = 10$	1.39	40.49	2.78	32.82/0.9489
$N_{CB} = 12$	1.64	48.04	3.25	32.82/0.9491
$N_{CB} = 14$	1.90	55.58	3.71	32.84/0.9499
$N_{CB} = 16$	2.16	63.13	4.18	32.91/0.9499
$N_{CB} = 18$	2.42	70.68	4.66	32.96/0.9508
$N_{CB} = 20$	2.67	78.23	5.12	<b>33.06/0.9512</b>

computational complexity, and the inference time is measured in seconds, indicating the actual elapsed time of processing a LF image. Ideally, a method positioned closer to the top-left corner of each plot is considered more efficient, as it achieves higher performance with fewer computational resources.

Our SkimLFSR network consistently excels across all three efficiency metrics. Notably, the most lightweight variant of SkimLFSR with  $N_{CB} = 4$  has already achieved a PSNR of 32.47 dB, outperforming all compared methods except M2MT-Net, and surpassing LF-DET by 0.06 dB. Remarkably, it does so with only 37% of the parameters, 35% of the FLOPs, and 28% of the inference time compared to LF-DET. This result aligns with our analysis in Section III-D and Table I, validating that compared to conventional spatial Transformers, Skim Transformers reduces computational redundancy through its skimming strategy while maintaining information integrity and emphasizing more pertinent information within the self-attention mechanism, embodying the “less is more” philosophy.

Compared to the best existing method, M2MT-Net, the smallest SkimLFSR variant that surpasses it is with  $N_{CB} = 8$ ,

achieving 32.80 dB, which is 0.09 dB higher. While the FLOPs and inference time are comparable (97% and 108%, respectively), this SkimLFSR model requires only 28% of the parameters, leading to a significantly lighter architecture. The reduced model size not only lowers the risk of overfitting but also enables easier scalability to deeper networks.

Indeed, as  $N_{CB}$  increases, SkimLFSR consistently improves in performance. The deepest variant with  $N_{CB} = 20$  reaches 33.06 dB, outperforming M2MT-Net and LF-DET by 0.35 dB and 0.65 dB, respectively. Remarkably, this model still uses only 67% of the parameters of M2MT-Net and is only 4% slower than LF-DET in inference time, while delivering significantly better results.

These results demonstrate that SkimLFSR achieves a compelling balance between performance and efficiency. It is capable of delivering lightweight variants, such as those with  $N_{CB} = 4$  and  $N_{CB} = 8$ , that offer strong performance under limited computational budgets. At the same time, it provides scalable, high-performance configurations such as  $N_{CB} = 20$ , which significantly outperform existing methods while maintaining a manageable model size and runtime. This adaptability makes SkimLFSR a practical and powerful solution for a wide range of real-world and high-demand LFSR applications.

### E. In-depth Analysis

To better understand the underlying mechanism driving SkimLFSR’s superior performance, we further conduct a series of in-depth analyses on the challenging  $4 \times$  scale.

1) *DSA Feature Visualization*: We first analyze the internal behavior of the Skim Transformer by visualizing the output features of its DSA modules. Fig. 7 displays the feature maps produced by  $DSA_1$  and  $DSA_2$  (first two columns), along with their differential activations ( $DSA_1 - DSA_2$  and  $DSA_2 - DSA_1$  in the last two columns). These differential maps reveal the exclusive focus areas of each DSA branch. The visualized samples are the same as those in Fig. 5.

A general trend is observed that, while both DSA branches exhibit overlapping activation regions, examination of the differential maps clearly demonstrates that the two branches possess distinct tendencies for discerning different disparity ranges and attending to complementary aspects of LF images.

Specifically, in Fig. 5 (a) *Perforated\_Metal\_3*,  $DSA_1 - DSA_2$  demonstrates strong activation on the perforated metal surface in the foreground, whereas  $DSA_2 - DSA_1$  predominantly highlights the background regions behind the metal board. This disparity separation is particularly noteworthy since the foreground and background regions exhibit markedly different disparity ranges, suggesting that SkimLFSR has developed an inherent capability to distinguish the perforated metal structure from the background.

The result in Fig. 5 (b) *Building\_Decoded* reveals a different specialization pattern. Here,  $DSA_1 - DSA_2$  appears to attend preferentially to background regions, including building walls, sky regions, and grass fields. Conversely,  $DSA_2 - DSA_1$  exhibits a pronounced tendency to focus on structural boundaries, particularly edges of the building and its windows.

Interestingly, an opposite pattern is observed in Fig. 5 (c) *Lego Knights*. In this case,  $DSA_1 - DSA_2$  primarily attends to structural edges, such as the knights and studs, while  $DSA_2 - DSA_1$  focuses on background regions. This reversal can be attributed to the fundamental differences between samples Fig. 5 (b) and (c): the former originates from a Lytro Illum camera capturing a far scene, while the latter is synthetically generated with a completely different camera configuration and presents near objects in a simulated environment. As a result, these two DSA branches demonstrate adaptive behavior, attending to content with different characteristics as well as the specific camera configuration.

These observations validate our hypothesis that the multi-branch architecture effectively mitigates disparity entanglement issues, enabling SkimLFSR to develop adaptive disparity-aware capabilities that facilitate comprehensive scene understanding during reconstruction. It is worth noting that, despite being trained solely on the regression-based LFSR task, in this study, considering separation of the perforated surface in (a) and locating the structures of building in (b) and lego in (c), SkimLFSR demonstrates emergent behavior resembling classification, suggesting implicit learning of semantics akin to classification tasks, like depth estimation [5] and shape extraction [4], highlighting the effectiveness of the proposed disparity disentanglement mechanism.

2) *t-SNE Visualization of DSA Features*: We further analyze SkimLFSR’s feature space using deep degradation representation (DDR), a technique originally proposed for interpreting single image super-resolution (SISR) models. In prior work [72], [73], it is discovered that by applying PCA [74] and t-SNE [75] to project the deep features into a two-dimensional space, well-trained SISR methods exhibit a strong clustering trend based on degradation types, suggesting that these methods have implicitly learned degradation as semantics, even though such information is not explicitly provided during training.

Inspired by this observation, we hypothesize that an effective LFSR method should similarly exhibit patterns related to disparity information in LF images. To validate this hypothesis, we perform the same technique to the three LFSR methods: EPIT [24], LF-DET [25], and M2MT-Net [27], on all the 167 samples from the BasicLFSR framework [60], as shown in Fig. 8. These samples are categorized into three camera configurations: the Lytro Illum camera group (blue), EPFL [68], INRIA [71]; the synthetic group (green), HCInew [69], HCIdold [70]; and the gantry-based camera group (red), STFgantry [21]. Each group is characterized by distinct disparity distributions due to different imaging setups: the Lytro Illum and gantry-based cameras employ different microlens configurations, while synthetic datasets simulate yet another unique angular distribution. To quantitatively assess the clustering trend, we compute the Calinski-Harabasz Index (CHI) [76] for each method as the metric, shown below the respective plots. The CHI score measures the ratio of between-cluster heterogeneity to within-cluster homogeneity; a higher CHI score indicates better cluster separability in the projected feature space.

Despite the clear disparity distinctions across camera con-

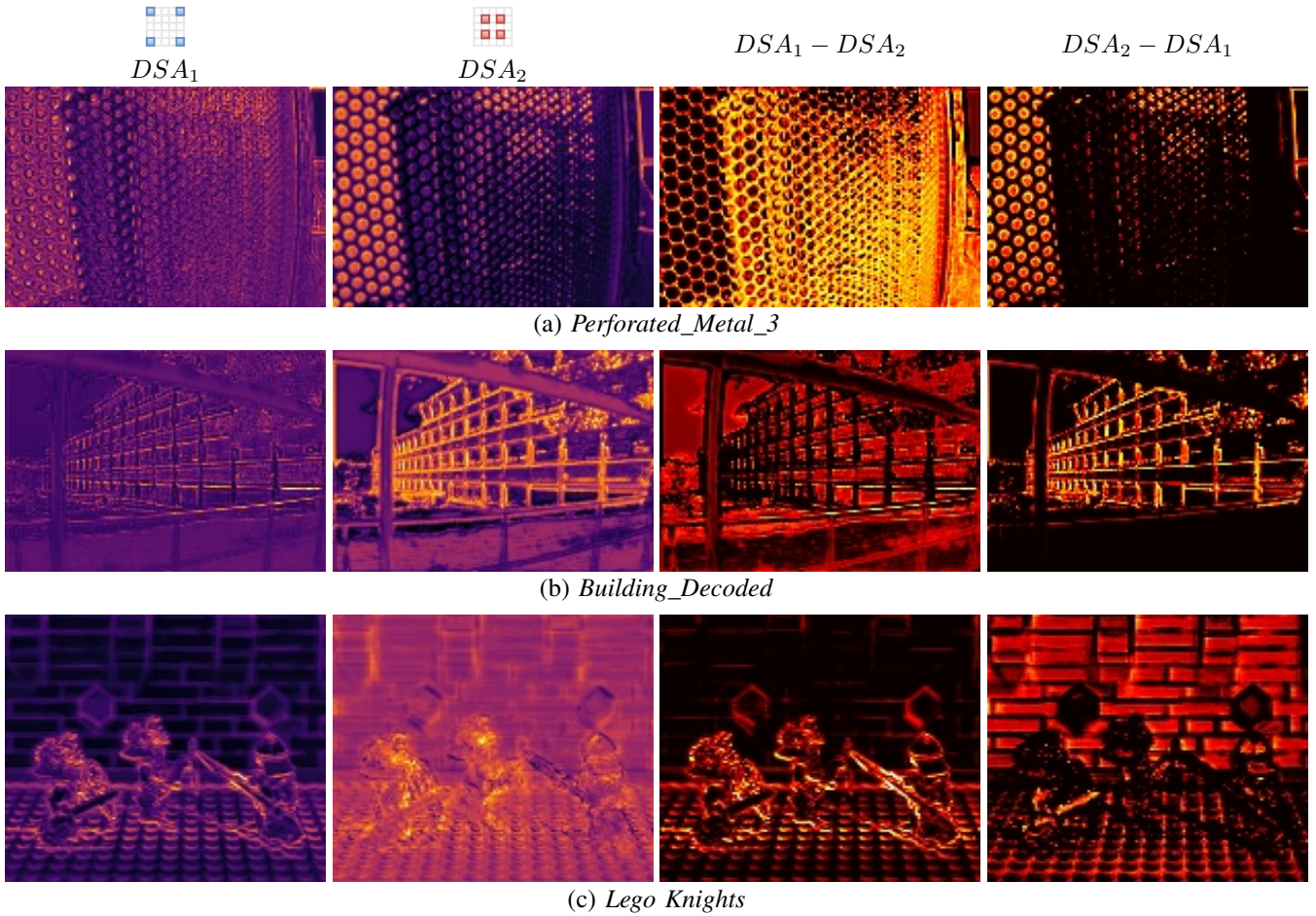


Fig. 7. Visualization of DSA feature maps. The first two columns display the outputs of the two DSA branches, respectively. The third and fourth columns present their differential activations, revealing the exclusive attention regions of each branch.

figuration groups, the feature visualizations in Fig. 8 show that the compared methods exhibit no evident clustering trend, suggesting a lack of disparity-aware representation. Among them, (b) LF-DET demonstrates the weakest separation (CHI: 6.48), with all three groups dispersed across the feature space. (a) EPIT (CHI: 17.25) and (c) M2MT-Net (CHI: 11.86) display a slight clustering trend by camera configurations, but substantial overlaps persist, with numerous outliers from each group intermingled with others. These results point to the potential disparity entanglement issue in these methods, where disparity-related cues are not effectively disentangled or captured in the learned feature representations.

In contrast, (d) SkimLFSR exhibits a clear and well-defined clustering pattern, with distinct boundaries separating the three groups and only minor overlaps. Its CHI score of 41.27 is substantially higher than those of the other methods, indicating that SkimLFSR has effectively learned to organize features based on disparity information.

This outcome strongly echoes our earlier observations in Fig. 7, where SkimLFSR demonstrates classification-like behavior despite being trained solely on a regression-based LFSR task. Whereas the previous analysis highlights SkimLFSR's ability to distinguish scene depths within a single LF image, the current t-SNE study reveals its capacity to differentiate camera configurations across LF images. Since scene depth

and camera configuration are the two primary factors influencing disparity variations in LF data, these results collectively indicate that SkimLFSR has developed a latent discriminative capability toward disparity information, i.e., disparity-aware, which finally contributes to its superior performance in LFSR tasks.

3) *Ablation study of Skimmed SAI Sets*: The configuration of the skimmed SAI sets in the DSA branches serves as critical prior knowledge for targeted disparity modeling in the Skim Transformer. To evaluate its impact, we conduct an ablation study, with results presented in Table IV.

We adopt the  $N_{CB} = 6$  model as the baseline, representing the full version of Skim Transformers in Column (a).

Columns (b) and (c) isolate the two individual skimmed SAI sets (blue and red) used in the baseline. Each subset underperforms the combined approach by 0.11 dB and 0.13 dB, respectively, demonstrating the advantage of combining different SAI sets to capture a broader disparity range.

Columns (d), (e), and (f) explore variants of (a), (b), and (c) using only half the number of SAIs. These configurations, which sample along a single diagonal line with a biased disparity coverage, lead to further degradation in performance: a drop of 0.18 dB for the dual-branch variant (Column (a) vs. (d)), and 0.28 dB for the single-branch variants (Column (a) vs. (e) and (f)). These results highlight the importance of both

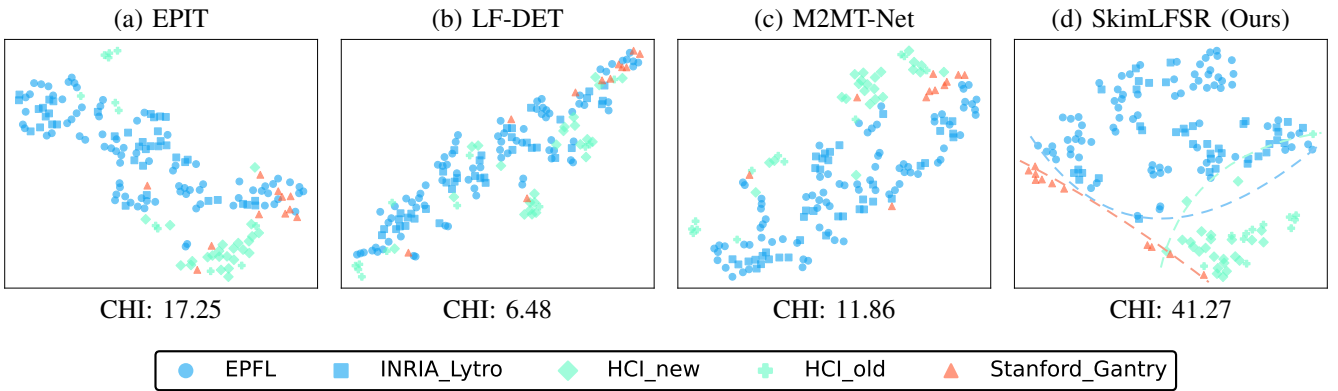


Fig. 8. Projected feature representation using t-SNE. Each plot contains 167 points, each of which represents a sample in the dataset. Colors indicate the light field camera configuration: Lytro Illum (blue), synthetic (green), and gantry-based (red). Higher CHI scores indicate better cluster separability.

TABLE IV  
COMPARISON OF DIFFERENT SKIMMED SAI SETS FOR SKIMLFSR ( $N_{CB} = 6$ ) OF  $4 \times$  LFSR.

Variant	(a)	(b)	(c)	(d)	(e)	(f)	(g)	(h)	(i)
PSNR/SSIM	32.58/0.9474	32.47/0.9451	32.45/0.9450	32.40/0.9449	32.30/0.9438	32.30/0.9435	32.05/0.9425	32.57/0.9469	32.50/0.9450
#Branches	2	1	1	2	1	1	1	3	1
#SAIs	4+4=8	4	4	2+2=4	2	2	1	4+4+4=12	25
#Parameters (M)	0.87	0.82	0.82	0.82	0.76	0.76	0.73	0.93	1.40
FLOPs (G)	25.38	25.03	25.03	25.33	24.97	24.97	24.94	25.75	25.62
Inference Time (s)	1.79	1.76	1.76	1.79	1.73	1.74	1.74	1.88	1.77

the quantity and spatial distribution of SAIs, as they directly influence the disparity coverage and, consequently, the model’s reconstruction quality.

Column (g) experiments with a minimal variant using only a single central SAI (yellow). In this setting, the angular scope of the attention score matrix is severely restricted, resulting in a substantial performance drop of 0.53 dB compared to the baseline. This highlights the necessity of the disparity modeling capabilities offered by DSA.

While the previous cases reduce either the number of DSA branches or the number of SAIs, each causing performance degradation, we find that merely increasing the number of SAIs does not necessarily lead to better results. Column (h) augments the baseline with a third DSA branch comprising central SAIs from each edge (green). Although this triple-branch variant introduces additional parameters and computational cost, it does not yield any noticeable performance improvement. This outcome suggests that the baseline configuration already provides sufficient disparity range coverage.

In a more extreme case, Column (i) consolidates all SAIs into a single DSA branch. This effectively reintroduces disparity entanglement, as the single branch must process all the SAI at once. Despite a 61% increase in model parameters, this configuration results in a 0.08 dB decrease in performance. This further confirms the importance of the information structure constructed by DSA branches over merely the amount of information involved.

Collectively, these results underscore the flexibility and effectiveness of the skimmed SAI design in DSA branches. More importantly, they highlight the need for strategic SAI con-

figuration to achieve comprehensive disparity coverage with minimal computational overhead, achieving “less is more”.

## V. CONCLUSION

In this paper, we presented SkimLFSR, a novel and efficient LFSR network that overcomes the challenge of disparity entanglement in LF image processing. The experimental results validated SkimLFSR’s “less is more” philosophy, demonstrating that SkimLFSR outperformed the state-of-the-art methods significantly by utilizing less but more pertinent information with reduced memory and computational complexity. Several in-depth analyses were conducted to reveal the underlying disparity-aware mechanisms of SkimLFSR.

Despite its success, our work has certain limitations. First, the disparity ranges for the Skim Transformers must be manually pre-specified. Although this is not a complex problem, it essentially introduces a prior into the network, which could potentially be made heuristic or learned in network optimization autonomously. Second, the LFSR datasets used in this study have limited angular resolution ( $5 \times 5$ ), which does not fully showcase SkimLFSR’s potential. Nevertheless, we believe that SkimLFSR could serve as a new paradigm for not only LFSR but also other LF-related tasks, allowing it to handle more complex angular resolutions.

## REFERENCES

- [1] J. Fiss, B. Curless, and R. Szeliski, “Refocusing plenoptic images using depth-adaptive splatting,” in *2014 IEEE international conference on computational photography (ICCP)*. IEEE, 2014, pp. 1–9.

[2] R. Ng, M. Levoy, M. Brédif, G. Duval, M. Horowitz, and P. Hanrahan, "Light field photography with a hand-held plenoptic camera," *Computer Science Technical Report CSTR*, vol. 2, no. 11, pp. 1–11, 2005.

[3] K. Yücer, A. Sorkine-Hornung, O. Wang, and O. Sorkine-Hornung, "Efficient 3d object segmentation from densely sampled light fields with applications to 3d reconstruction," *ACM Transactions on Graphics (TOG)*, vol. 35, no. 3, p. 22, 2016.

[4] S. Heber, W. Yu, and T. Pock, "Neural EPI-Volume Networks for Shape from Light Field," in *Proceedings of the IEEE International Conference on Computer Vision*, 2017, pp. 2271–2279.

[5] T.-C. Wang, A. A. Efros, and R. Ramamoorthi, "Occlusion-aware depth estimation using light-field cameras," in *Proceedings of the IEEE International Conference on Computer Vision*, 2015, pp. 3487–3495.

[6] W. Chao, X. Wang, Y. Wang, G. Wang, and F. Duan, "Learning sub-pixel disparity distribution for light field depth estimation," *IEEE Transactions on Computational Imaging*, vol. 9, pp. 1126–1138, 2023.

[7] Y. Ding, Z. Chen, Y. Ji, J. Yu, and J. Ye, "Light Field-Based Underwater 3D Reconstruction via Angular Re-Sampling," *IEEE Transactions on Computational Imaging*, vol. 9, pp. 881–893, 2023.

[8] T.-C. Wang, J.-Y. Zhu, E. Hiroaki, M. Chandraker, A. A. Efros, and R. Ramamoorthi, "A 4D light-field dataset and CNN architectures for material recognition," in *European Conference on Computer Vision*. Springer, 2016, pp. 121–138.

[9] Z. Lu, H. W. Yeung, Q. Qu, Y. Y. Chung, X. Chen, and Z. Chen, "Improved image classification with 4d light-field and interleaved convolutional neural network," *Multimedia Tools and Applications*, vol. 78, no. 20, pp. 29211–29227, 2019.

[10] H. Sheng, S. Zhang, X. Liu, and Z. Xiong, "Relative location for light field saliency detection," in *2016 IEEE International Conference on Acoustics, Speech and Signal Processing (ICASSP)*. IEEE, 2016, pp. 1631–1635.

[11] M. Zhang, W. Ji, Y. Piao, J. Li, Y. Zhang, S. Xu, and H. Lu, "Lfnet: Light field fusion network for salient object detection," *IEEE Transactions on Image Processing*, vol. 29, pp. 6276–6287, 2020.

[12] G. Chen, H. Fu, T. Zhou, G. Xiao, K. Fu, Y. Xia, and Y. Zhang, "Fusion-Embedding Siamese Network for Light Field Salient Object Detection," *IEEE Transactions on Multimedia*, vol. 26, pp. 984–994, 2024.

[13] H. Verinaz-Jadan, P. Song, C. L. Howe, A. J. Foust, and P. L. Dragotti, "Shift-invariant-subspace discretization and volume reconstruction for light field microscopy," *IEEE Transactions on Computational Imaging*, vol. 8, pp. 286–301, 2022.

[14] H. Verinaz-Jadan, C. L. Howe, P. Song, F. Lesept, J. Kittler, A. J. Foust, and P. L. Dragotti, "Physics-based deep learning for imaging neuronal activity via two-photon and light field microscopy," *IEEE Transactions on Computational Imaging*, vol. 9, pp. 565–580, 2023.

[15] M. Levoy, R. Ng, A. Adams, M. Footer, and M. Horowitz, "Light field microscopy," in *AcM Siggraph 2006 Papers*, 2006, pp. 924–934.

[16] R. Raghavendra, K. B. Raja, and C. Busch, "Presentation attack detection for face recognition using light field camera," *IEEE Transactions on Image Processing*, vol. 24, no. 3, pp. 1060–1075, 2015.

[17] Z. Ji, H. Zhu, and Q. Wang, "LFHOG: A discriminative descriptor for live face detection from light field image," in *2016 IEEE International Conference on Image Processing (ICIP)*. IEEE, 2016, pp. 1474–1478.

[18] F. H. a. K. C. a. G. Wetzstein, F.-C. Huang, D. P. Luebke, and G. Wetzstein, "The light field stereoscope," in *SIGGRAPH Emerging Technologies*, 2015, pp. 21–24.

[19] M. Broxton, J. Flynn, R. Overbeck, D. Erickson, P. Hedman, M. Duvall, J. Dourgarian, J. Busch, M. Whalen, and P. Debevec, "Immersive light field video with a layered mesh representation," *ACM Transactions on Graphics (TOG)*, vol. 39, no. 4, pp. 86–1, 2020.

[20] P. Debevec, "Experimenting with light fields," <https://blog.google/products/google-ar-vr/experimenting-light-fields/>, accessed: 2024-07-29.

[21] V. Vaish and A. Adams, "The (new) stanford light field archive," *Computer Graphics Laboratory, Stanford University*, vol. 6, no. 7, p. 3, 2008.

[22] Raytrix, "3d light field camera technology," <https://raytrix.de/>, accessed: 2024-07-29.

[23] Wikipedia contributors, "Lytro — Wikipedia, the free encyclopedia," <https://w.wiki/7G9s>, accessed: 2024-07-29.

[24] Z. Liang, Y. Wang, L. Wang, J. Yang, S. Zhou, and Y. Guo, "Learning non-local spatial-angular correlation for light field image super-resolution," in *Proceedings of the IEEE/CVF International Conference on Computer Vision*, 2023, pp. 12376–12386.

[25] R. Cong, H. Sheng, D. Yang, Z. Cui, and R. Chen, "Exploiting Spatial and Angular Correlations With Deep Efficient Transformers for Light Field Image Super-Resolution," *IEEE Transactions on Multimedia*, vol. 26, pp. 1421–1435, 2024.

[26] Z. Liang, Y. Wang, L. Wang, J. Yang, and S. Zhou, "Light field image super-resolution with transformers," *IEEE Signal Processing Letters*, vol. 29, pp. 563–567, 2022.

[27] Z. Z. Hu, X. Chen, V. Y. Y. Chung, and Y. Shen, "Beyond Subspace Isolation: Many-to-Many Transformer for Light Field Image Super-resolution," *IEEE Transactions on Multimedia*, pp. 1–15, 2024.

[28] C. Dong, C. C. Loy, K. He, and X. Tang, "Learning a deep convolutional network for image super-resolution," in *European Conference on Computer Vision*, vol. 8689, 2014, pp. 184–199.

[29] R. Timofte, V. De Smet, and L. Van Gool, "Anchored neighborhood regression for fast example-based super-resolution," in *Proceedings of the IEEE international conference on computer vision*, 2013, pp. 1920–1927.

[30] J. Yang, J. Wright, T. S. Huang, and Y. Ma, "Image super-resolution via sparse representation," *IEEE transactions on image processing*, vol. 19, no. 11, pp. 2861–2873, 2010.

[31] J. Kim, J. K. Lee, and K. M. Lee, "Accurate Image Super-Resolution Using Very Deep Convolutional Networks," in *IEEE Computer Society Conference on Computer Vision and Pattern Recognition (CVPR)*, 2016, pp. 1646–1654.

[32] Y. Zhang, Y. Tian, Y. Kong, B. Zhong, and Y. Fu, "Residual dense network for image super-resolution," in *Proceedings of the IEEE Conference on Computer Vision and Pattern Recognition*, 2018, pp. 2472–2481.

[33] Y. Zhang, K. Li, K. Li, L. Wang, B. Zhong, and Y. Fu, "Image super-resolution using very deep residual channel attention networks," in *European Conference on Computer Vision*, 2018, pp. 286–301.

[34] A. Esmailzehi, M. O. Ahmad, and M. Swamy, "Srnnss: a deep light-weight network for single image super resolution using spatial and spectral information," *IEEE Transactions on Computational Imaging*, vol. 7, pp. 409–421, 2021.

[35] R. Wu, T. Yang, L. Sun, Z. Zhang, S. Li, and L. Zhang, "SeeSR: Towards Semantics-Aware Real-World Image Super-Resolution," Nov. 2023. [Online]. Available: <http://arxiv.org/abs/2311.16518>

[36] J. Johnson, A. Alahi, and L. Fei-Fei, "Perceptual losses for real-time style transfer and super-resolution," in *European Conference on Computer Vision*. Springer, 2016, pp. 694–711.

[37] M. S. M. Sajjadi, B. Schölkopf, and M. Hirsch, "EnhanceNet: Single Image Super-Resolution Through Automated Texture Synthesis," in *IEEE International Conference on Computer Vision*, 2017, pp. 4491–4500.

[38] A. Dosovitskiy, L. Beyer, A. Kolesnikov, D. Weissenborn, X. Zhai, T. Unterthiner, M. Dehghani, M. Minderer, G. Heigold, S. Gelly, J. Uszkoreit, and N. Houlsby, "An image is worth 16x16 words: Transformers for image recognition at scale," in *International Conference on Learning Representations*, 2021. [Online]. Available: <https://openreview.net/forum?id=YicbFdNTTy>

[39] H. Chen, Y. Wang, T. Guo, C. Xu, Y. Deng, Z. Liu, S. Ma, C. Xu, C. Xu, and W. Gao, "Pre-trained image processing transformer," in *Proceedings of the IEEE/CVF Conference on Computer Vision and Pattern Recognition*, 2021, pp. 12299–12310.

[40] J. Liang, J. Cao, G. Sun, K. Zhang, L. Van Gool, and R. Timofte, "Swinir: Image restoration using swin transformer," in *Proceedings of the IEEE/CVF International Conference on Computer Vision*, 2021, pp. 1833–1844.

[41] Z. Liu, Y. Lin, Y. Cao, H. Hu, Y. Wei, Z. Zhang, S. Lin, and B. Guo, "Swin transformer: Hierarchical vision transformer using shifted windows," in *Proceedings of the IEEE/CVF International Conference on Computer Vision*, 2021, pp. 10012–10022.

[42] X. Chen, X. Wang, J. Zhou, Y. Qiao, and C. Dong, "Activating more pixels in image super-resolution transformer," in *Proceedings of the IEEE/CVF Conference on Computer Vision and Pattern Recognition*, 2023, pp. 22367–22377.

[43] Y. Zhou, Z. Li, C.-L. Guo, S. Bai, M.-M. Cheng, and Q. Hou, "SRFormer: Permuted Self-Attention for Single Image Super-Resolution. [Online]. Available: <http://arxiv.org/abs/2303.09735>

[44] X. Zhang, H. Zeng, S. Guo, and L. Zhang, "Efficient long-range attention network for image super-resolution," in *Computer Vision–ECCV 2022: 17th European Conference, Tel Aviv, Israel, October 23–27, 2022, Proceedings, Part XVII*. Springer, 2022, pp. 649–667.

[45] H. Sun, W. Li, J. Liu, H. Chen, R. Pei, X. Zou, Y. Yan, and Y. Yang, "Coser: Bridging image and language for cognitive super-resolution," in *Proceedings of the IEEE/CVF Conference on Computer Vision and Pattern Recognition*, 2024, pp. 25868–25878.

[46] R. Wu, T. Yang, L. Sun, Z. Zhang, S. Li, and L. Zhang, "Seesr: Towards semantics-aware real-world image super-resolution," in *Proceedings of the IEEE/CVF conference on computer vision and pattern recognition*, 2024, pp. 25456–25467.

[47] R. Rombach, A. Blattmann, D. Lorenz, P. Esser, and B. Ommer, "High-resolution image synthesis with latent diffusion models," in *Proceedings of the IEEE/CVF conference on computer vision and pattern recognition*, 2022, pp. 10684–10695.

[48] A. Radford, J. W. Kim, C. Hallacy, A. Ramesh, G. Goh, S. Agarwal, G. Sastry, A. Askell, P. Mishkin, J. Clark *et al.*, "Learning transferable visual models from natural language supervision," in *International conference on machine learning*. PMLR, 2021, pp. 8748–8763.

[49] Y. Zhang, X. Huang, J. Ma, Z. Li, Z. Luo, Y. Xie, Y. Qin, T. Luo, Y. Li, S. Liu *et al.*, "Recognize anything: A strong image tagging model," in *Proceedings of the IEEE/CVF Conference on Computer Vision and Pattern Recognition*, 2024, pp. 1724–1732.

[50] P. Esser, R. Rombach, and B. Ommer, "Taming transformers for high-resolution image synthesis," in *Proceedings of the IEEE/CVF conference on computer vision and pattern recognition*, 2021, pp. 12873–12883.

[51] H. W. F. Yeung, J. Hou, J. Chen, Y. Y. Chung, and X. Chen, "Fast light field reconstruction with deep coarse-to-fine modeling of spatial-angular clues," in *The European Conference on Computer Vision (ECCV)*, Sep. 2018, pp. 137–152.

[52] Y. Yoon, H.-G. Jeon, D. Yoo, J.-Y. Lee, and I. S. Kweon, "Light-field image super-resolution using convolutional neural network," *IEEE Signal Processing Letters*, vol. 24, no. 6, pp. 848–852, 2017.

[53] H. W. F. Yeung, J. Hou, X. Chen, J. Chen, Z. Chen, and Y. Y. Chung, "Light Field Spatial Super-Resolution Using Deep Efficient Spatial-Angular Separable Convolution," *IEEE Transactions on Image Processing*, vol. 28, no. 5, pp. 2319–2330, 2019.

[54] J. Jin, J. Hou, J. Chen, and S. Kwong, "Light field spatial super-resolution via deep combinatorial geometry embedding and structural consistency regularization," in *Proceedings of the IEEE/CVF Conference on Computer Vision and Pattern Recognition*, 2020, pp. 2260–2269.

[55] Y. Wang, L. Wang, J. Yang, W. An, J. Yu, and Y. Guo, "Spatial-angular interaction for light field image super-resolution," in *European Conference on Computer Vision*. Springer, 2020, pp. 290–308.

[56] G. Liu, H. Yue, J. Wu, and J. Yang, "Intra-Inter View Interaction Network for Light Field Image Super-Resolution," *IEEE Transactions on Multimedia*, vol. 25, pp. 256–266, 2021.

[57] Y. Chen, G. Jiang, Z. Jiang, M. Yu, and Y.-S. Ho, "Deep light field super-resolution using frequency domain analysis and semantic prior," *IEEE Transactions on Multimedia*, vol. 24, pp. 3722–3737, 2021.

[58] Z. Cheng, Y. Liu, and Z. Xiong, "Spatial-Angular Versatile Convolution for Light Field Reconstruction," *IEEE Transactions on Computational Imaging*, vol. 8, pp. 1131–1144, 2022.

[59] Z. Hu, X. Chen, H. W. F. Yeung, Y. Y. Chung, and Z. Chen, "Texture-Enhanced Light Field Super-Resolution With Spatio-Angular Decomposition Kernels," *IEEE Transactions on Instrumentation and Measurement*, vol. 71, pp. 1–16, 2022.

[60] Y. Wang, L. Wang, G. Wu, J. Yang, W. An, J. Yu, and Y. Guo, "Disentangling light fields for super-resolution and disparity estimation," *IEEE Transactions on Pattern Analysis and Machine Intelligence*, vol. 45, no. 1, pp. 425–443, 2023.

[61] V. Van Duong, T. N. Huu, J. Yim, and B. Jeon, "Light Field Image Super-Resolution Network via Joint Spatial-Angular and Epipolar Information," *IEEE Transactions on Computational Imaging*, pp. 1–16, 2023.

[62] S. Wang, T. Zhou, Y. Lu, and H. Di, "Detail-preserving transformer for light field image super-resolution," in *Proceedings of the AAAI Conference on Artificial Intelligence*, vol. 36, 2022, pp. 2522–2530.

[63] W. Shi, J. Caballero, F. Huszar, J. Totz, A. P. Aitken, R. Bishop, D. Rueckert, and Z. Wang, "Real-Time Single Image and Video Super-Resolution Using an Efficient Sub-Pixel Convolutional Neural Network," in *2016 IEEE Conference on Computer Vision and Pattern Recognition (CVPR)*. IEEE, Jun. 2016, pp. 1874–1883.

[64] X. Chu, Z. Tian, B. Zhang, X. Wang, and C. Shen, "Conditional positional encodings for vision transformers," *arXiv preprint arXiv:2102.10882*, 2021.

[65] K. He, X. Zhang, S. Ren, and J. Sun, "Deep Residual Learning for Image Recognition," in *2016 IEEE Conference on Computer Vision and Pattern Recognition (CVPR)*, 2016, pp. 770–778.

[66] Z. Chen, Y. Zhang, J. Gu, L. Kong, and X. Yang, "Recursive generalization transformer for image super-resolution," *arXiv preprint arXiv:2303.06373*, 2023.

[67] Github, "Basiclfsr: Open source light field toolbox for super-resolution," <https://github.com/ZhengyuLiang24/BasicLFSR>, accessed: 2024-07-29.

[68] M. Rerábek and T. Ebrahimi, "New Light Field Image Dataset," *8th International Conference on Quality of Multimedia Experience (QoMEX)*, pp. 1–2, 2016.

[69] K. Honauer, O. Johannsen, D. Kondermann, and B. Goldluecke, "A dataset and evaluation methodology for depth estimation on 4d light fields," in *Asian Conference on Computer Vision*. Springer, 2016, pp. 19–34.

[70] S. Wanner, S. Meister, and B. Goldluecke, "Datasets and benchmarks for densely sampled 4D light fields," in *Vision, Modelling and Visualization (VMV)*, vol. 13, 2013, pp. 225–226.

[71] M. Le Pendu, X. Jiang, and C. Guillemot, "Light field inpainting propagation via low rank matrix completion," *IEEE Transactions on Image Processing*, vol. 27, no. 4, pp. 1981–1993, 2018.

[72] Y. Liu, A. Liu, J. Gu, Z. Zhang, W. Wu, Y. Qiao, and C. Dong, "Discovering distinctive "semantics" in super-resolution networks," *arXiv preprint arXiv:2108.00406*, 2021.

[73] X. Kong, X. Liu, J. Gu, Y. Qiao, and C. Dong, "Reflash dropout in image super-resolution," in *Proceedings of the IEEE/CVF Conference on Computer Vision and Pattern Recognition*, 2022, pp. 6002–6012.

[74] H. Hotelling, "Analysis of a complex of statistical variables into principal components," *Journal of educational psychology*, vol. 24, no. 6, p. 417, 1933.

[75] Y. Liu, H. Zhao, J. Gu, Y. Qiao, and C. Dong, "Evaluating the Generalization Ability of Super-Resolution Networks," *IEEE Transactions on Pattern Analysis and Machine Intelligence*, vol. 45, no. 12, pp. 14497–14513, Dec. 2023.

[76] T. Caliński and J. Harabasz, "A dendrite method for cluster analysis," *Communications in Statistics-theory and Methods*, vol. 3, no. 1, pp. 1–27, 1974.



**Zeke Zexi Hu** is currently a Ph.D. candidate at the School of Computer Science, University of Sydney, Australia. He received his bachelor's degree from South China Agricultural University, China in 2014 and his Master of Philosophy degree from the University of Sydney in 2020. His research focuses on image processing and visual tracking. He has authored and co-authored papers in academic journals and conferences, including IEEE TMM, TCSVT, TVCG, TIM, ICIP, etc.



**Haodong Chen** received the Bachelor of Computer Science and Technology (Honours) from the University of Sydney, Australia, where he is currently pursuing the Ph.D. degree in Computer Science. His research focuses on applying artificial intelligence and bio-inspired sensors to computer vision and computer graphics, including image segmentation, edge detection, and 3D reconstruction.



**Hui Ye** earned a Bachelor of Engineering from Chengdu University of Technology, China, and a Master of Engineering from Monash University, Australia. He later received a Master of Philosophy from the University of Sydney, where he is currently pursuing a Ph.D. in Computer Science. His research focuses on remote sensing, semantic segmentation, and vision-language models.



**Xiaoming Chen** holds a B.Sc. degree (with Distinction) from Royal Melbourne Institute of Technology and a Ph.D. degree from the University of Sydney, Australia. He has a combined experience in industry and academia. He has been with National University of Singapore, Nanyang Technological University, Singapore, CSIRO Australia, Technicolor Research, IBM Corporation, and University of Science and Technology of China (USTC). He is now a Professor at the School of Computer and Artificial Intelligence, Beijing Technology and Business University (BTBU), China, and a researcher at the University of Sydney, Australia. His research interests include immersive media computing, virtual reality, bio-inspired event processing, and related applications. His work has been published in journals and conferences including IEEE Trans. Vis. Comput. Graph., IEEE Trans. Image Process., IEEE Trans. Circuits Syst. Video Technol., IEEE Trans. Mult., IEEE VR, ACM MM, ECCV, AAAI, etc.



**Vera Yuk Ying Chung** received her B.S. degree in Computing and Information Systems from the University of London, UK, in 1995, and her Ph.D. degree in Computer Engineering from the Queensland University of Technology, Australia in 2000. She is a Senior Lecturer at the School of Computer Science, University of Sydney, Australia. Her research interests are in the areas of multimedia computing and virtual reality. Her work has been published in journals and conferences including IEEE Trans. on Image Processing, IEEE Trans. Vis. Comput. Graph., IEEE Trans. Mult., IEEE Trans. Circuits Syst. Video Technol., NeurIPS, ECCV, etc.



**Yiran Shen** is professor in School of Software, Shandong University. He received his BE in communication engineering from Shandong University, China and his PhD degree in computer science and engineering from University of New South Wales. He published regularly at top-tier conferences and journals. Generally speaking, his research interest is sensing and computing for immersive systems. He is a senior member of IEEE.



**Weidong Cai** received the Ph.D. degree in computer science from the Basser Department of Computer Science, The University of Sydney, Australia, in 2001. He is currently an Associate Professor and the Director of Multimedia Laboratory, School of Computer Science, Faculty of Engineering, The University of Sydney. His research interests include multimedia computing, computer vision, medical image computing, machine learning, image/video processing, pattern recognition, and computer graphics.